

Fluid Core Size of Mars from Detection of the Solar Tide

C. F. Yoder,* A. S. Konopliv,* D. N. Yuan, E. M. Standish,
W. M. Folkner

The solar tidal deformation of Mars, measured by its k_2 potential Love number, has been obtained from an analysis of Mars Global Surveyor radio tracking. The observed k_2 of 0.153 ± 0.017 is large enough to rule out a solid iron core and so indicates that at least the outer part of the core is liquid. The inferred core radius is between 1520 and 1840 kilometers and is independent of many interior properties, although partial melt of the mantle is one factor that could reduce core size. Ice-cap mass changes can be deduced from the seasonal variations in air pressure and the odd gravity harmonic J_3 , given knowledge of cap mass distribution with latitude. The south cap seasonal mass change is about 30 to 40% larger than that of the north cap.

There are few geophysical constraints on the interior structure of Mars except the identification of meteorites (shergottites) thought to come from Mars, which are iron rich relative to an Earth-like mantle. The existence of remnant crustal magnetism (1) and the polar moment of inertia (2) imply that Mars has a substantial iron core that was liquid at one time. The size of the core is loosely constrained by the observed moment of inertia. However, factors such as mantle composition, temperature change with increasing depth, and average crustal thickness contribute to the uncertainty in core size. Crustal thickness has been estimated to range from 50 to 100 km (3, 4). On the basis of Mars Global Surveyor (MGS) tracking data, Smith *et al.* (5, 6) reported a solution for the tidal Love number k_2 of 0.055 ± 0.008 , which implies the Martian core has solidified. Any value for $k_2 < \sim 0.10$ would indicate a solid core. We have analyzed over 3 years of MGS Doppler and range data acquired during gravity calibration and mapping (February 1999 to April 2002) and find a much larger Love number that is indicative of a liquid core. The Love number solution is stable when subsets of the data and parameter combinations are considered and input models are modified. k_2 is a scale factor multiplying the tidal gravitational potential of Mars and is detected remotely from the perturbations in the MGS spacecraft orbit. A larger k_2 indicates a greater deformation of the figure of Mars by the gravitational pull of the Sun and hence a less rigid Mars (7).

We determined the tidal Love number, equatorial precession rate, seasonal variations in the gravity harmonics J_2 and J_3 , and seasonal variations in rotation rate in a

joint solution for these and other model parameters. These parameters included a static gravity field (up to degree 85), spin axis direction of Mars, the mass of Mars, the masses of Phobos and Deimos, atmospheric drag, solar radiation pressure, infrared and reflected radiation from the surface of Mars and spacecraft positions. The solution combined information from MGS data and Mars Pathfinder and Viking Lander range and Doppler data (8). The Love number and seasonal gravity estimates depend mainly on the MGS data, whereas the lander tracking tends to fix Mars' pole position, mean precession rate, and seasonal spin variations. Our model also includes Mars nutation (9, 10). If nutation is omitted, it can substantially change the seasonal solution for J_2 , where-as the Love number change is about 10%.

The detection of tides on Mars depends on finding reliable, long-period signatures (longer than the spacecraft-orbit period) in their effects on the orbit of MGS, because short-period changes are too small to be observable (11). The tidal potential is given by

$$U = \frac{GR^2 M_{\text{sun}}}{r'^3} [k_{20} P_{20}(\vartheta) + k_{21} P_{21}(\vartheta) \cos\alpha + k_{22} P_{22}(\vartheta) \cos 2\alpha] \quad (1)$$

where α and ϑ are the longitude and colatitude, respectively, of the Sun as seen from Mars; P_{2m} functions are the associated Legendre polynomials of degree 2 and order m ; and k_{20} , k_{21} , and k_{22} characterize the longitude independent ($m = 0$), diurnal ($m = 1$), and semidiurnal ($m = 2$) tides. Other parameters are planet radius, R ; solar mass, M_{sun} ; Mars-Sun distance, r' ; and gravitational constant, G . One would expect the Love number constants k_{20} , k_{21} , and k_{22} to be equal because of spherical symmetry, in which case we would replace k_{20} , k_{21} , and k_{22} with k_2

in Eq. 1. The effect of the tides causes changes in the spacecraft orbital elements that are different for each Love number contribution. The changes in the semimajor axis, orbital eccentricity, argument of pericenter, and mean anomaly due to tides are smaller than the contributions due to the uncertainty in the atmospheric drag. In order to minimize the effect of atmospheric drag on solutions for k_2 , the drag model solves for a new drag coefficient for each MGS orbit and thus effectively absorbs the influence of the along-track residual signature (12). So, the tidal signatures are clearest in the orbital inclination and longitude of the node. A crucial tidal signature is a secular drift in spacecraft orbit inclination related to the Sun-synchronous spacecraft orbit (13), which is primarily driven by the k_{22} tide.

The long-period changes in MGS orbit inclination, I , and node, Ω , arise from a variety of sources, including direct gravitational action of the Sun, solid-body tides, solar-induced atmospheric thermal tides, seasonal changes in even zonal gravity coefficients, motion of the rotation axis of Mars (secular precession and small periodic oscillations or nutations), and solar radiation pressure. The tidal force on the MGS spacecraft is about 1/10 of the direct solar gravitational force (fig. S2). Because the solar mass and position are accurately known, the uncertainty in the solar gravitational force is much smaller than the tidal force. Similarly, the uncertainties in the nutations (14) and the forces due to solar light pressure and light emitted from the martian surface are small compared with the tidal force. Seasonal changes in Mars gravity primarily affect the zonal harmonic gravity coefficients J_n . The even zonal harmonics do not affect the inclination but significantly affect the orbit node. The odd harmonics weakly affect the orbit inclination and have a negligible effect on the node. Thus, the only secular or long-period changes we need to be concerned with for I and Ω are solid-body tides and the seasonal even zonal gravity.

The inclination change is given by (15)

$$\frac{dI_{k_{22}}}{dt} = k_{22} n' T \sin I \left(\cos^4(\epsilon/2) \sin 2(\Omega - L') + \frac{1}{2} \sin^2 \epsilon \sin 2(\Omega - \psi) \right) \quad (2)$$

where $T = 3/4(n'/n)(R/a)^5(a'/r')^3 \approx 5.2 \times 10^{-5}(a'/r')^3$ and other parameters are the orbital longitude of the Mars, L' ; the longitude of Mars' equator on Mars orbit, ψ ; the Mars orbit mean motion, n' ; obliquity, $\epsilon = 25.189^\circ$; and semimajor axes a' of Mars and a of MGS (16). The inclination rate is nearly secular because the MGS orbit is Sun-synchronous, making $\Omega - L' \approx 30^\circ$ nearly constant, and the second term in Eq. 2 is small (17). This results in a secular

Jet Propulsion Laboratory, California Institute of Technology, Pasadena, CA 91109, USA.

*To whom correspondence should be addressed. E-mail: Charles.F.Yoder@jpl.nasa.gov (C.F.Y.); Alex.Konopliv@jpl.nasa.gov (A.S.K.)

drift in the orbit inclination of $d\dot{I}/dt \approx 1.7k_{22}$ m/day. The inclination-rate signature is most apparent in the Doppler data when the orbit is nearly face-on as seen from Earth, having amplitude

$$\delta I(t) \approx n \cos(L - \Omega) \cos \beta \approx$$

$$1.5k_{22}(\Delta t/\text{day}) \cos(L - \Omega) \cos \beta \text{ mm/s} \quad (3)$$

where β is the angle between the spacecraft orbit normal and the Mars-to-Earth direction (Fig. 1) and L is the longitude of the MGS orbit. The k_{22} tidal force also has a signature on the nodal rate that is 1/20 of the inclination rate because of the near polar geometry (18).

The k_{21} tidal component acting on the MGS orbit causes an annual signature of the inclination rate (18), but, because the signature is proportional to $\cos I$, it is also 1/20 the size of the k_{22} contribution. However, the effect of the k_{21} tide on the node is proportional to $\sin I$ and can be significant for some orbital orientations:

$$\frac{d\Omega_{k_{21}}}{dt} \equiv$$

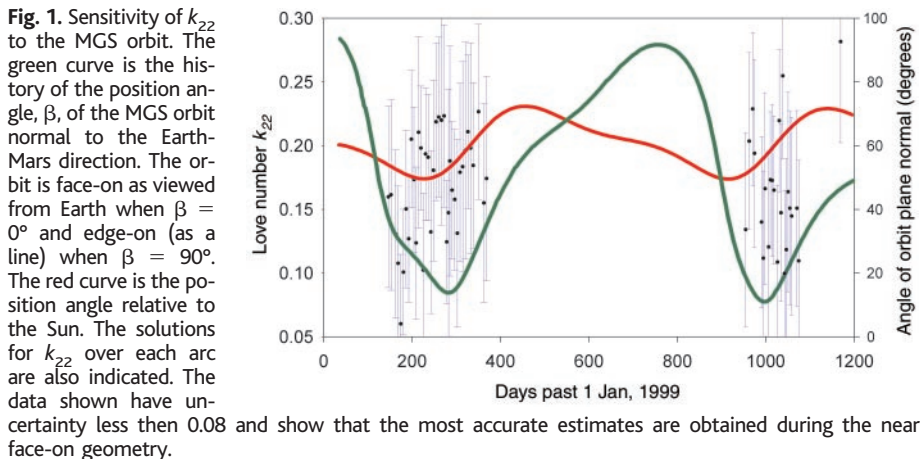
$$-k_{21}n'T \sin I \sin \varepsilon (\cos \varepsilon \cos(\Omega - \psi) + \frac{1}{2} \cos^2(\varepsilon/2) \cos(\Omega + \psi - 2L')) \quad (4)$$

The orbit node rate is also best determined by the Doppler data during face-on encounters. However, the k_{21} contribution from Eq. 4 happens to vanish during face-on geometry (19). Also, the nodal rate due to k_{21} tides is hard to separate from the nodal rate due to the seasonal changes in the even zonal gravity harmonics, which are given by (20, 21):

$$\frac{d\Omega_{\delta J}}{dt} \equiv n'(\delta J_2 + f_4 \delta J_4 + \dots)/J_2 \quad (5)$$

The estimated seasonal δJ_2 inferred from air pressure changes (22) is

$$\delta J_2 \approx 1.8 \times 10^{-9} \sin(\ell' + 22^\circ) + 1.5 \times 10^{-9} \cos(2\ell' + 2^\circ) \quad (6)$$



which results in a nodal rate signature that is comparable in amplitude to the k_{21} contribution.

Our results are determined by estimating only k_{22} while constraining k_{20} and k_{21} to be equal to the solution of k_{22} . Tidal k_{21} is not well determined for the reasons above. Tidal k_{20} is poorly determined because the k_{20} tide can mimic much larger seasonal changes in J_2 (22). In separate tests estimating k_{20} and k_{21} we find k_{22} is much more accurate with formal uncertainties of $\sigma(k_{20}) \approx 20\sigma(k_{22})$ and $\sigma(k_{21}) \approx 7\sigma(k_{22})$, and the solution for k_{21} is unstable (23).

The solutions for k_2 (as represented by k_{22} , see Table 1), precession constant, and moment of inertia (24) are

$$k_2 = 0.153 \pm 0.017 \quad (7)$$

$$d\dot{\theta}/dt = -7597 \pm 25 \times 10^{-3} \text{ arc sec/year} \quad (7)$$

$$C/MR_e^2 = 0.3650 \pm 0.0012$$

The uncertainties in Eq. 7 are five times as large as the formal standard deviation for the Love number and 10 times as large as the formal standard deviation for the precession to account for model deficiencies and colored noise (25). Table 1 shows that the solution for k_{22} is stable for various subsets of the MGS data and with and without solutions for seasonal changes in both the odd and even zonal gravity harmonics. Figure 1 shows estimates for k_{22} for each individual data segment, with only estimates shown that have estimated uncertainty < 0.08 . This shows that the strongest contribution to the estimate of k_{22} results from the data arcs that have a nearly face-on geometry.

The estimated k_2 includes the effects of both solid-body (k_2^s) and atmospheric (k_2^a) tides. The atmospheric tide can be estimated with the use of knowledge of the semidiurnal pressure change at the surface (26, 27). We have used both atmospheric global circulation models (GCM) model estimates and Mars Pathfinder pressure data (fig. S3). The semidiurnal pressure variation ranges from 0.5 to 1% of the mean pressure, and the maximum occurs about 1.5 hours before local noon. We estimate the contribution of the

atmospheric tide to k_2 is about 0.004 to 0.008, implying that the solid-body Love number in Eq. 7 should be reduced by a similar amount. The effects of solid-body friction (i.e., phase lag) and fluid core nutation increase the effective Love number by about 0.002 (14, 16). Thus, the Love number in Eq. 7 should be reduced by 0.002 to 0.006.

The solid-body tide includes elastic and inelastic components. The elastic component can be compared with model calculations of tidal deformation (22, 28–30). The inelastic component depends on the tidal quality factor Q . Observation of the decay of the orbit of Phobos provides a measure of the quantity k_2^s/Q (31). Combining our estimate of k_2 (here, biased downward to $k_2 = 0.149 \pm 0.017$) with the Phobos orbit decay measurements gives a new estimate for Q of:

$$Q = 92 \pm 11 \quad (8)$$

For Earth, the inelastic solid-body tide is estimated to be less than $3k_2/Q$ for the semidiurnal lunar tide (32), so for Mars we estimate that the inelastic correction is less than 0.005 for k_2 . To account for this effect, we shall adopt a k_2 (elastic) value of 0.145 ± 0.017 .

Mars interior. The tidal Love number depends primarily on the product of mantle rigidity and mantle thickness combined with the size and state of the core. Suites of models for the interior structure of Mars (i.e., density, rigidity, and bulk modulus) have been constructed with the use of Earth's known profile as a starting point (15, 22). The composition of the mantle is parameterized by the molar fraction $\chi_M = \text{Mg}/(\text{Mg} + \text{Fe})$ of magnesium relative to iron (for Earth, χ_M is ~ 0.89). The temperature profile of the mantle is assumed to be the same as that for Earth at the same pressure plus a constant temperature offset ΔT . The crustal thickness, h_{cr} , is assumed to range between 50 and 100 km (3, 4). The core density is parameterized by the sulfur content [defined by $\chi_c = \text{FeS}/(\text{Fe} + \text{FeS})$] and is determined by the three free parameters (χ_M , ΔT , and h_{cr}) and the known total mass of Mars (33). These three-parameter

Table 1. Representative solutions for k_{22} from data subsets. GCO is the gravity calibration orbit phase before mapping phase (February to March 1999), and MPF indicates the Mars Pathfinder. Each of the two solutions with a portion of the MGS mapping data represents values for each of the MGS face-on geometries.

Solution	k_{22}
MGS + MPF + Viking	0.153 ± 0.017
MGS + MPF + Viking (no δJ_2)	0.164 ± 0.017
MGS (GCO + mapping)	0.161 ± 0.017
MGS (GCO + mapping to Oct. 2000)	0.160 ± 0.025
MGS (GCO + mapping after Oct. 2000)	0.176 ± 0.031

models do not explore the full range of possible martian structures. Some researchers obtain similar results (26), whereas others construct a stiffer mantle with smaller k_2 (27).

The calculated Love number and polar moment of inertia for a range of models as a function of core radius are shown in Fig. 2. Figure 2A shows an estimated k_2 that con-

strains the core radius to be $1520 \text{ km} \leq R_c \leq 1840 \text{ km}$. The allowed range of models for Mars interior are limited by total moment and k_2 and defined by χ_M ; ΔT and h_{cr} thickness are constrained to be in the box in Fig. 2B. We can infer that the molar fractions satisfy

$$\chi_M \approx [83 - \Delta T / 100 \text{ K} - (h_{cr} - 50 \text{ km}) / 8 \text{ km}] \pm 3\% \quad (9)$$

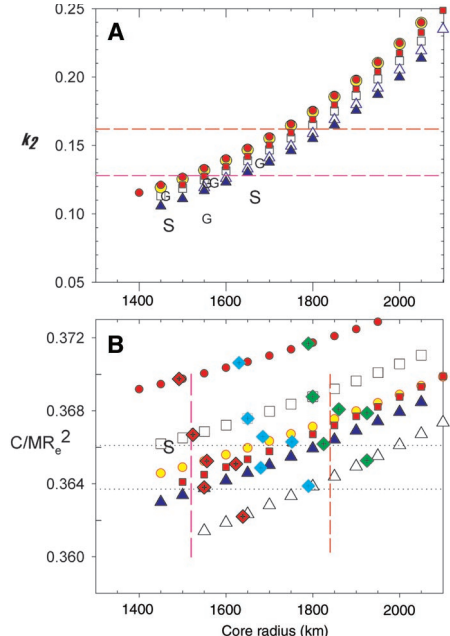


Fig. 2. Model estimates of the elastic Love number k_2 (A) and moment of inertia C/MR_e^2 (B) versus core radius for a representative suite of structural models of Mars. These models vary χ_M [85% (triangles), 80% (boxes), and 75% (circles)] and ΔT [200 K (red and yellow), 0 K (white), and -200 K (blue)]. Crustal thickness is 50 km except for $\chi_M = 75\%$, $\Delta T = 200\text{ K}$, and $h_{cr} = 100\text{ km}$ (yellow circles). Diamonds correspond to core $\chi_c = \text{Fe}/(\text{Fe} + \text{FeS})$ of 25% (red), 50% (cyan), and 75% (green) in Fig. 2B. Constraints on C/MR_e^2 (dotted lines) from Eq. 7 and the inferred elastic $k_2 = 0.145 \pm 0.17$ (dashed lines) are also shown.

and $15\% \leq \chi_c \leq 75\%$. The inferred composition of Mars is close to that of Earth if it has a cold interior and thin crust. Models with mantles that are more iron rich than that of Earth are preferred either if the crust is as thick as 100 km or if the thermal profile is as warm as or warmer than Earth. The core size also implies that the core composition is not pure iron but mixed with a substantial light component such as sulfur or hydrogen (28). A small χ_c tends to be more consistent with a hot, iron-rich mantle, whereas a large χ_c tends to be more consistent with a cold, Earth-like mantle. The lower bound on sulfur fraction in the core in Eq. 9 is near the estimated upper bound based on relative abundance arguments (26–28).

An alternative interpretation of the large observed k_2 is that the mantle is softer than the assumed elastic solid model because of partial melt at depth. The Love number k_2 for the Moon (34–36) is about 20% larger than expected, and a similar interpretation may be the explanation. A molten fraction of 5% by volume would result in a reduction in rigidity of 10 to 15% and an increase in k_2 by a similar amount. This would have the effect of reducing the inferred core radius by 100 to 150 km.

Seasonal gravity. Seasonal changes in zonal gravity coefficients arise from Mars' CO₂ ice-cap growth and decay and are sensitive to the size and shape (i.e., variation in cap thickness with latitude) of each ice cap. Changes in air pressure can be used to estimate the total change in ice-cap mass (north and south). If both caps

were the same size and their histories were 180° out of phase, then pressure would not change. The observed change in pressure is thought to be due primarily to the difference in the northern and southern cap sizes, although phasing cannot be entirely discounted. Smith *et al.* (5), with the use of Mars Orbiter Laser Altimetry (MOLA) from MGS to Mars surface, estimated that the annual changes in the volumes of the northern and southern ice caps are about equal and that the cap thickness varies nearly linearly and increases with latitude.

Our estimates of seasonal changes in J_2 and J_3 have been obtained as a periodic series in which the amplitudes of the sine and cosine coefficients (8) are solution parameters and can be used to test different models of cap formation. To investigate the robustness of the periodic series solution, we have made separate solutions with only annual sine and cosine terms estimated and with independent corrections to J_2 and J_3 estimated for each data segment, as was done by Smith *et al.* (5) (Fig. 3). The J_3 histories from the different solutions are similar. The J_2 histories are different but are more consistent during intervals when the spacecraft orbit is nearly face-on to Earth. This is possibly because the J_2 corrections are primarily determined from observations of changes in the orbital node and can correlate with variations in the atmospheric drag that also affect the node. We consider the estimated annual and semiannual corrections to be internally consistent and consistent with the corrections estimated from changes in air pressure (e.g., Eq. 6). The estimated corrections at shorter periods are suspect, particularly the 1/3-year term, which is much larger than predicted. The J_3 changes primarily affect the spacecraft orbit eccentricity and pericenter angle (21). Determination of these is best during edge-on geometry and is poorest during face-on geometry. However, the orbit is never exactly face-on, and thus one can resolve the J_3 changes over the whole data interval.

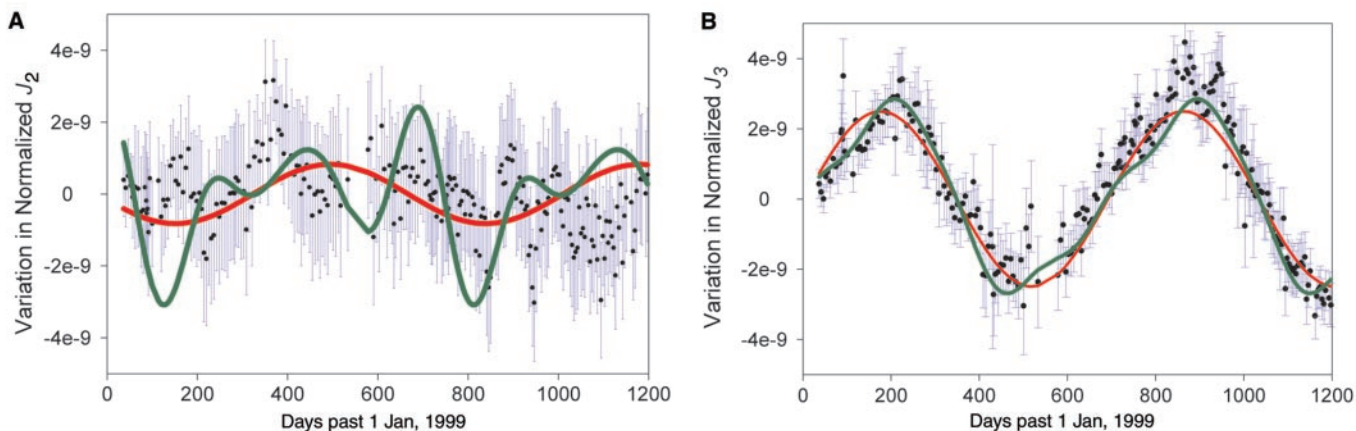


Fig. 3. Seasonal normalized J_2 (A) and J_3 (B) solutions ($\tilde{J}_n = J_n / \sqrt{2n+1}$) using two different techniques. The curves are global solutions (including tides and 85° gravity field) for annual (red) and annual plus 1/2, 1/3, and 1/4

year terms (green). The 4- to 6-day arc solutions are obtained by holding the other gravity harmonics fixed. The segment solutions are kept stable by adopting a priori constraints of 2×10^{-9} for \tilde{J}_2 and 3×10^{-9} for \tilde{J}_3 .

The estimated seasonal correction to J_3 is primarily annual and is given by

$$\delta J_3 = - \left(\begin{array}{l} (6.59 \pm 0.28) \sin(\ell' - 7^\circ) \\ + (1.34 \pm 0.26) \sin(2\ell' - 15^\circ) \\ + (0.25 \pm 0.24) \sin(3\ell' - 12^\circ) \\ - (0.43 \pm 0.22) \sin(4\ell' + 10^\circ) \end{array} \right) \times 10^{-9} \quad (10)$$

and the uncertainties listed are five times larger than the formal estimates.

The influence of ice-cap mass distributions on the predicted gravity coefficients was explored with the use of four different thickness profiles as a function of latitude, ranging from a flat cap (model A) to a conical cap (model C)

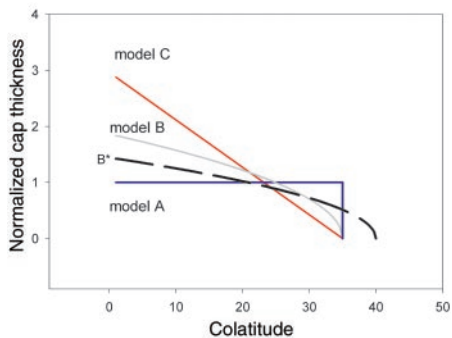


Fig. 4. Cap mass thickness for four different spherical cap models. Model assumptions are given in Table 2.

Fig. 5. Ice cap mass histories for four ice-cap density distribution models. $L_s \equiv \ell' + 251^\circ + 11\sin\ell'$ and is 0° at northern spring equinox.

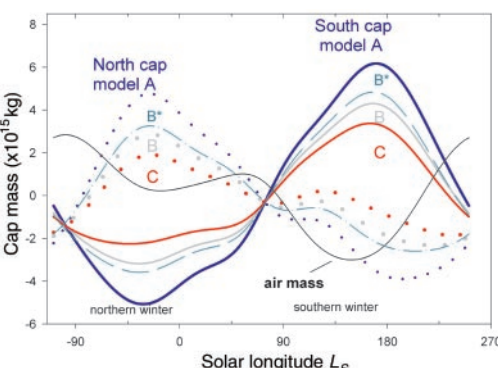


Table 3. Seasonal rotation changes. $\delta\Omega(J_2)$ is inferred from δJ_2 with the use of $d\Omega/dt = n'\delta J_2/J_2$. If the rotation changes are due to just δJ_2 , then there is a linear relationship (15): $\delta\Omega = K\delta\phi$ and $K =$

$9/4(C_m/MR^2)(R/a)^2(n/\frac{dt}{dt})\cos\phi \approx -0.41$. The variable rotation results are consistent within the

uncertainties of Folkner et al. (2), whereas our results are slightly different because of data weighting techniques and editing. The j terms are $\times 10^{-3}$ arc sec.

Terms $\cos\ell'$ $\sin\ell'$	MGS	Viking + MPF	MGS + Viking + MPF	Viking pressure (1, 7)	MGS $\delta\Omega(J_2)$
$j = 1$	398 -194	433 -169	434 -211	439 -184	-186 -41
$j = 2$	-216 -283	-71 -89	-106 -129	-6 -204	7 124
$j = 3$	-6 10	-53 24	-51 11	3 -25	
$j = 4$	24 78	-36 -19	-21 -30	2 -10	

(Fig. 4). For each distribution, the ice-cap mass history is derived by fitting the actual δJ_3 inferred from the observed δJ_3 and the known air pressure variation. The estimated scaling factors for true versus observed δJ_3 for the different thickness profiles are given in Table 2. Figure 5 shows the resulting time histories for the four models. The mass change in the northern cap inferred from the models ranges from 3.7×10^{15} to 8.6×10^{15} kg. The southern cap mass change is about 30 to 40% larger than the northern cap mass change. The northern cap density ranges from 1250 to 2900 kg/m³ if we use the MOLA volume estimate for the northern cap (5). This result tends to favor model C because

solid CO₂ density is 1600 kg/m³. Models A or B could be acceptable if the mass partially resides in a subsurface reservoir or if MOLA underestimates cap volume (37). The maximum north cap thickness is 0.4 m for a solid, uniform CO₂ sheet (i.e., model A).

There are several other tests of the preferred ice-cap model, but none are conclusive. We have estimated δJ_5 in addition to δJ_3 and found that the ratio $\delta J_5/\delta J_3 = 0.6 \pm 0.2$. This result is consistent with cap thickness decreasing with decreasing latitude (5, 38) (Table 2 and table S3). However, the δJ_3 estimate in Eq. 10 agrees with a GCM model calculation (39) for δJ_3 (Smith et al. found δJ_3 amplitude was $\sim 7.7 \times 10^{-9}$), recognizing that the estimated δJ_3 has absorbed variations in all odd zonal gravity harmonics. This agreement suggests that models A or B* best fit this constraint. The estimated annual and semianual correction to J_2 is given by

$$\begin{aligned} \delta J_2 = & (1.81 \pm 1.02) \times 10^{-9} \sin(\ell' + 12^\circ) \\ & + (2.32 \pm 0.94) \times 10^{-9} \cos(2\ell' - 3^\circ) \end{aligned} \quad (11)$$

Again, the uncertainties listed are five times larger than the formal uncertainties. The observed δJ_2 signal also suggests that the flat distribution is favored.

Seasonal rotation. MGS can also detect the seasonal rotation changes of Mars (Table 3) by effectively tracking the relative position of the large gravitational features such as Tharsis. The annual term observed with MGS agrees quite well with the Viking Lander estimate (2) and a model estimate derived from air pressure changes (22). Contribution from annual changes in atmospheric zonal winds to rotation are apparently small. The semiannual term gives significantly different results by all three methods, and winds might be significant here. These results qualitatively agree with a GCM calculation (40) that finds that zonal winds contribute about 4% to the annual term and 30% to the semiannual term.

References and Notes

1. M. H. Acuna et al., *Science* **284**, 790 (1999).
2. W. M. Folkner et al., *Science* **278**, 1749 (1997).
3. M. T. Zuber et al., *Science* **287**, 1788 (2000).
4. D. L. Turcotte et al., *J. Geophys. Res. (Planets)* **107**, 1 (2002).
5. D. E. Smith, M. T. Zuber, G. A. Neumann, *Science* **294**, 2141 (2002).
6. They (5) find maximum north and south ice-cap volumes are both $\sim 3 \times 10^{15}$ m³ and cap density is ~ 910 kg/m³. They also find $\delta J_2/(1/2 \text{ year}) \approx (2.2 \pm 0.8)\cos(2\ell' - 20^\circ)$.
7. J. Wahl, in *A Handbook of Physical Constants: Global Earth Physics*, T. J. Ahrens, Ed. [American Geophysical Union (AGU), Washington, DC, 1995], vol. 1, pp. 40–46.
8. The MGS, Pathfinder, and Viking Lander data are processed with the same least-squares estimation technique and observational models as described in D. N. Yuan, W. L. Sjogren, A. S. Konopliv, A. B. Kucinskas, *J. Geophys. Res.* **106**, 23377 (2001). The MGS data is processed in segments of 4- to 6-day intervals; for each segment, the epoch spacecraft position, atmospheric drag, spacecraft maneuvers, and observational calibrations are estimated that pertain specifically to that data segment. All the MGS segments are then combined together with one Pathfinder data arc and one Viking Lander data arc. For the landers, the arc-specific parameters include lander position and

range bias estimation. In addition to the segment or arc-specific parameters, the solution for parameters common to most arcs includes the Love number, rotation parameters, Mars satellite parameters, the mean spherical harmonic gravity field to degree 85, and seasonal J_2 and J_3 as

$$\delta J_n = \sum_{j=1}^4 (C_j^n \cos j\ell' + S_j^n \sin j\ell').$$

9. Starting from an orientation model of Mars similar to that of Folkner *et al.* (2), the rotational parameters we estimate are the epoch obliquity (ε) and longitude of the Mars pole (ψ), the precession rate of the pole ($d\psi/dt$), the obliquity rate ($d\varepsilon/dt$), the rotation rate ($d\phi/dt$), and the seasonal variations in rotation angle as a periodic series

$$\delta\phi = \sum_{j=1}^4 (C_j \cos j\ell' + S_j \sin j\ell')$$

where ℓ' is the Mars mean anomaly. The rigid-body nutation model is fixed to that of (10).

10. R. D. Reasenberg *et al.*, *J. Geophys. Res.* **82**, 369 (1977).

11. A. S. Konopliv *et al.*, *Geophys. Res. Lett.* **23**, 1857 (1996).

12. The drag model uses six flat plates to represent the spacecraft bus, antenna, and solar arrays with orientation provided by spacecraft telemetry. The atmospheric density is given by the Mars GRAM 3.4 model in C. J. Justus, D. L. Johnson, B. F. James, *NASA Tech. Memo. No. 108513* (1996). We also tested solving for a drag coefficient only once per day, and this did not change the results.

13. The orbit inclination is chosen such that $d\Omega/dt = -3/2\cos(J_2(R/a')^2)n = n'$. Also, the MGS orbit elements are: $a = 3796$ km, $e = 0.0084$, period = 1.96 hours, and $I = 92.9^\circ$.

14. The nutations of Mars pole ($\delta\varepsilon$ and $\delta\psi$) result in the following changes in orbit inclination relative to a space-fixed reference frame (15, 22):

$$\frac{dI_{\text{nut}}}{dt} \approx -n'[\delta\varepsilon\cos(\Omega-\psi) - \delta\psi\sin(\Omega-\psi)]$$

The principal annual term for rigid-body response is $\delta\varepsilon = 0.0$ and $\delta\psi = -0.259\sin\ell'$. This reduces the secular rate by about 10%. The fluid core can further reduce rate by up to 1%.

15. C. F. Yoder, *Icarus* **117**, 250 (1995).

16. A phase lag ($= 1/Q$) can be introduced in the angle arguments in Eq. 2 in order to account for solid friction. For

example $2(\Omega - L')$ is replaced with $2(\Omega - L') - 1/Q$. This effect reduces the observed signature by about 1%.

17. The inclination drift does cause a secular acceleration in the node ($d\Omega_\delta/dt \approx -n'\tan(\delta)$) that has about the same amplitude as the secular change in inclination after ~ 20 days. Thus, both node and inclination drift contribute to the global Love number solution. However, space craft maneuvers aimed at desaturation of the momentum wheels and maintaining orbit geometry may limit the sensitivity to long-term orbit changes.
18. $d\Omega_{k_2}/dt \approx k_{21}n'T\cos[(\varepsilon/2)\cos^2(\ell/2)\cos(2(\Omega - L') + 1/2\sin^2(\varepsilon/2)\cos^2(\Omega - \psi)], d\Omega_{k_3}/dt \approx k_{21}n'T\cos[(\varepsilon/2)\cos(\Omega - \psi) + 1/2\cos^2(\varepsilon/2)\sin(\Omega + \psi - 2L')]$
19. Let $\Omega = L' + \theta$. It happens that $L' - \psi \approx 260^\circ$ during face-on (August 1999 and June 2001). We find $[\cos(\Omega - \psi) + 1/2\cos^2(\varepsilon/2)\cos(\Omega + \psi - L')] = 0$ for $\sin\theta \approx 0.5$, corresponding to 2:00 p.m. local Mars time.
20. C. F. Yoder *et al.*, *Nature* **303**, 757 (1983).
21. The scalar factors $f_n(x)$ are $x = \sin^2\ell$, $f_4 = 5/8(R/a)^2(7x - 4)$, and $f_6 = -5/8(R/a)^4[7 - 54x + (62 + 5/8)x^2]$. The effect of odd J_n on spacecraft orbit e and argument of pericenter ω is obtained from the equation $dp/dt + i\omega_p = 3/2\sin(R/a)^3f_3\delta J_{\text{odd}}$
22. $\delta J_{\text{odd}} = \sum_{j=1}^4 (f_{2j+1}/f_3)\delta J_{2j+1}$
The variable $p = e\exp(-i\omega)$ while $i = \sqrt{-1}$, $w_0 \approx 3\pi(R/a)^2f_3$, and the scalars are $f_3 = (1 - 5/4x)$, $f_5 = -5/16(R/a)^2[8 - 28x + 21x^2]$, and $f_7 = 35/64(R/a)^4[8 - 54x + 99x^2 - (53 + 5/8)x^3]$. Also, the mean orbit eccentricity $e \approx (R/a)(J_3/J_2)$ is due primarily to this forcing.
23. C. F. Yoder *et al.*, *J. Geophys. Res.* **102**, 4065 (1997).
24. Solutions for k_{21} range from -0.1 to 0.1 .
25. The latest estimate for (unnormalized) J_2 is $1.985683(3) \times 10^{-3}$ (Mars $R_e = 3394.2$ km), and the precession rate is [see (2, 10, 22)] $d\psi/dt = [-7606(0.365MR_e^2/C) \times 10^{-3}] \text{ arc sec/year} + d\psi/dt_p + d\psi/dt_g$, where the contribution from Jupiter is $d\psi/dt_p = -0.2 \times 10^{-3}$ arc sec/year and geodetic precession is $d\psi/dt_g = +6.7 \times 10^{-3}$ arc sec/year.
26. In the estimation process, the Doppler data are treated as uncorrelated measurements, i.e., white noise. Solar plasma, troposphere, and ionosphere can cause correlations in the measurements that are impractical to account for in a least-squares estimation process.
27. R. M. Haberle *et al.*, *J. Geophys. Res. (Planets)* **104**, 8957 (1999).
28. The semidiurnal surface pressure field due to solar heating can be approximated by $\delta P_{22}\sin(\Omega)\cos(2\alpha + 41^\circ)$, where δP_{22} is the equatorial amplitude (Pathfinder pressure data indicate $\delta P_{22} \approx 0.011P_0$). The global

mean pressure $P_0 \approx 5.6$ mbar, and the hour angle $\alpha = 0$ at midnight (see SOM Text for more details). However, the estimate from one GCM (29) has the same phase, but $1/2$ the amplitude. The atmospheric $k_2 \approx 3.08(1 + k'_2)R^2/gM_{\text{sun}}(R/a')^3\delta P_{22}\sin(2(\Omega - L' + 41^\circ)/\sin 2(\Omega - L'))$. Surface gravity $g = 0.372 \text{ m/s}^2$ and the load $k'_2 \approx -0.8k_2$. Thus, $k_2 \approx 0.008$.

29. E. Groten *et al.*, *Astron. J.* **111**, 1388 (1996).
30. F. Sohl, T. Spohn, *J. Geophys. Res.* **102**, 1613 (1997).
31. V. N. Zharkov, Gudkova, *Phys. Earth Planet. Inter.* **117**, 407 (2000).

32. C. F. Yoder, in *A Handbook of Physical Constants: Global Earth Physics* (AGU, Washington, DC, 1995), vol. 1, pp. 1–31.
33. R. D. Ray *et al.*, *Nature* **381**, 585 (1996).

34. Compressed mean core density at core temperature ranges from 5.2 g/cm^3 [high pressure Fe(0.9)S (and $\chi_c = 1$)] to 7.5 g/cm^3 ($\chi_c = 0$), and this poses limits on core size represented by the upper and lower bounds on core radius shown in model calculations in Fig. 2.
35. J. O. Dickey *et al.*, *Science* **265**, 482 (1994).
36. A. S. Konopliv *et al.*, *Icarus* **150**, 1 (2001).

37. The most recent lunar Love number from Lunar Prospector (35) is $k_2 = 0.025 \pm 0.003$. The model estimate (34) is $k_2 = 0.022$ without partial melt at depth.
38. The mass change in the southern cap ranges from 5.7×10^{15} (model C) to 11.3×10^{15} kg (model A). The corresponding density (5) is 1900 to 3800 kg/m^3 . This suggests that at least the south cap volume is larger than reported.

39. The ratio J_3/J_2 is 0.224 (model A), 0.436 (model B), and 0.561 (model C). The ratio f_5/f_3 is 0.97 for MGS (21) (table S1).
40. E. Smith *et al.*, *J. Geophys. Res.* **104**, 1885 (1999).
41. E. Van den Akker *et al.*, *J. Geophys. Res. (Planets)* **105**, 24563 (2000).

42. We thank J. G. Williams, C. K. Shum, and V. Dehant for thoughtful reviews and J. T. Schofield for advice and Pathfinder pressure data. The research described in this paper was carried out by the Jet Propulsion Laboratory, California Institute of Technology, under a contract with NASA.
43. **Supporting Online Material**
www.sciencemag.org/cgi/content/full/1079645/DC1
SOM Text
Figs. S1 to S6
Tables S1 to S3

22 October 2002; accepted 19 February 2003

Published online 6 March 2003;

10.1126/science.1079645

Include this information when citing this paper.

REPORTS

Band Structure and Fermi Surface of Electron-Doped C_{60} Monolayers

W. L. Yang,^{1,3} V. Brouet,^{3,1,4} X. J. Zhou,³ Hyoung J. Choi,⁵ Steven G. Louie,^{2,5} Marvin L. Cohen,^{2,5} S. A. Kellar,³ P. V. Bogdanov,³ A. Lanzara,³ A. Goldoni,⁶ F. Parmigiani,⁷ Z. Hussain,¹ Z.-X. Shen^{3*}

C_{60} fullerides are challenging systems because both the electron-phonon and electron-electron interactions are large on the energy scale of the expected narrow band width. We report angle-resolved photoemission data on the band dispersion for an alkali-doped C_{60} monolayer and a detailed comparison with theory. Compared to the maximum bare theoretical band width of 170 meV, the observed 100-meV dispersion is within the range of renormalization by electron-phonon coupling. This dispersion is only a fraction of the integrated peak width, revealing the importance of many-body effects. Additionally, measurements on the Fermi surface indicate the robustness of the Luttinger theorem even for materials with strong interactions.

Exhibiting properties such as high transition temperature superconductivity (1) and anti-ferromagnetism (2), C_{60} -based fullerides are

ideal model compounds for exploring key conceptual issues in strongly correlated physics (3). As in typical molecular systems, the

bands formed through the overlap of the C_{60} molecular levels are expected to be narrow, on the order of 0.5 eV for the lowest unoccupied molecular orbital (LUMO)-derived band (4). On the other hand, the Coulomb repulsion between electrons is larger [more than 1 eV (5)], and some phonons have very high energies [up to 200 meV (3)] comparable to the expected bandwidth of half-filling. This set of parameters suggests a totally non-conventional behavior: On one hand, the strong electron-electron interaction predicts the proximity of metal-insulator transitions of the Mott-Hubbard type, whereas the high phonon frequencies predict a breakdown of the adiabatic approximation. In angle-integrated photoemission measurements (AIPES), the width of the LUMO peak, which naively corresponds to the band width, appears much wider (~ 1 eV) than the theo-